International Journal of Heat and Fluid Flow 21 (2000) 278–284

International Journal of
HEAT AND
FLUID FLOW

www.elsevier.com/locate/ijhff

Flowfield characteristics of swept struts in supersonic annular flow

K.E. Williams [a], F.B. Gessner [b,*]

[a] *Adroit Systems Inc., Bellevue, WA 98004, USA*

[b] *Department of Mechanical Engineering, University of Washington, P.O. Box 352600, Seattle, WA 98195, USA*

Received 30 August 1999; accepted 1 February 2000

Abstract

Supersonic flow over four, circumferentially equidistant, diamond-shaped swept struts positioned between a concentric cylindrical cowl and centerbody is examined from both experimental and numerical points of view. Experimental cross flow vectors and cross-planar pitot pressure and static pressure contours are compared with their numerical counterparts downstream of the strut trailing edge. Numerical results are also presented which show shock wave and expansion fan patterns generated at each strut/endwall intersection in order to demonstrate the full complexity of the flow. The numerical results are analyzed to show that computed limiting streamlines on the strut, cowl and centerbody surfaces are compatible with corner and shock generated vortices observed in the flow. Comparisons between predicted and measured contours downstream of the strut trailing edge indicate that the prescribed zero-equation (isotropic eddy viscosity) turbulence model performs well outside the wake region behind a strut, but not within the wake itself. © 2000 Elsevier Science Inc. All rights reserved.

Keywords: Supersonic turbulent flow; Strut/endwall juncture flow; Streamwise vortices; Shock/boundary layer interactions

1. Introduction

Supersonic flow past a strut mounted on an endwall generates a complex vortical flow pattern near the strut/endwall intersection. Recent studies by Williams et al. (1995) and Williams and Gessner (1996), based on supersonic flow past diamond-shaped struts mounted between concentric cylinders, have shown that four distinct vortices are formed in the vicinity of each strut/endwall intersection. These vortices consist of two horseshoe vortices generated at the leading and trailing edges of the strut and two, contra-rotating corner vortices formed along the compression and expansion faces of the strut which propagate as shown in Fig. 1.

In reference to applications, diamond-shaped struts are one means of supporting the outer cowl of the supersonic through-flow fan engine (Franciscus, 1987; Barnhart, 1988). This type of strut configuration with lenticular (curved) surfaces to minimize shock losses has also been proposed as a means of supporting swirling jet fuel injectors in some combustor applications (Heiser and Pratt, 1993). Local flow behavior in these geometries is influenced to some extent by compression face corner vortices that have propagated into the wake region behind each strut, as shown in Fig. 1. More specifically, these vortices can distort flow at the compressor face of the supersonic through-flow fan engine and can lead to non-uniform spray dispersal downstream of a strut-mounted, swirling jet fuel injector. These propagating vortices can also be a complicating factor when simulating oblique shock wave/tip vortex interactions of the type that occur in high-speed flight (Rizzetta, 1995; Smart and Kalkoran, 1995), especially if the height-to-chord ratio of the vortex generator (strut) in the model simulation is relatively small, which could lead to the paths of tip and corner induced vortices being in relatively close proximity downstream of the strut trailing edge.

These examples are intended to illustrate that vortices generated by a strut/endwall intersection may have an important bearing on the downstream flow within a particular geometry and affect overall performance. The purpose of this paper is to present the results of a study concerned with the effect of strut sweep on local flow behavior in the vicinity of a strut/endwall intersection. This work represents an extension of an earlier related computational and experimental study in which supersonic flow about unswept, endwall-mounted struts was investigated (Williams and Gessner, 1998).

2. Experimental program

Experiments were conducted in a continuous, open-loop supersonic flow facility whose design and operation are discussed by Williams et al. (1994). The test section is composed of a rotatable centerbody (83.0 mm OD) positioned concentrically within a stationary cowl (118.6 mm OD) to yield an annular gap width of 17.8 mm. Four symmetric, equally spaced, diamond-shaped struts were mounted on the centerbody as shown in Fig. 2. The struts were made from stainless steel with faces polished to a near-mirror finish. The strut

---

[*] Corresponding author. Tel.: +1-206-543-5090; fax: +1-206-685-8047.
E-mail address: gessnerf@u.washington.edu (F.B. Gessner).

0142-727X/00/$ - see front matter
PII: S0142-727X(00)00010-2

height (h) and chord width (c) are 17.8 and 25.7 mm, respectively, yielding a strut height-to-chord ratio $h/c = 0.7$ and a dimensionless gap width $\Delta r/c = 0.7$, where Δr is a radial coordinate measured from the centerbody surface, as shown in Fig. 2. The maximum strut thickness (t) is 3.18 mm, yielding a 7.1° half-wedge angle for the compression and expansion faces of the strut. Sweep was accomplished by holding the cross section of the swept strut the same as that of the unswept strut (dimensions c and t the same for both struts) and, in effect, rotating the unswept strut about its midchord intersection point with the centerbody (at $\Delta r/c = 0, x/c = 0.5$) to a sweep back angle of 45°, and then adjusting its length to intersect the cowl and centerbody surfaces, as shown in Fig. 3.

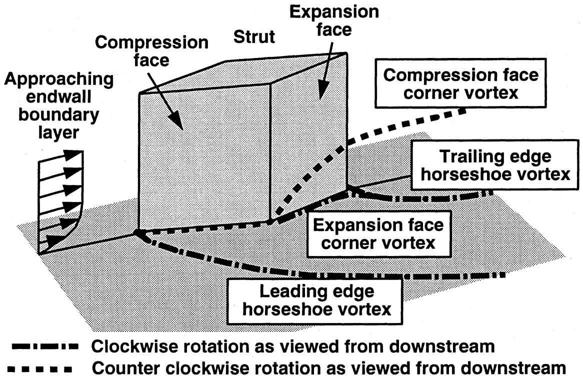

Fig. 1. Observed vortices as a strut/endwall intersection in supersonic flow.

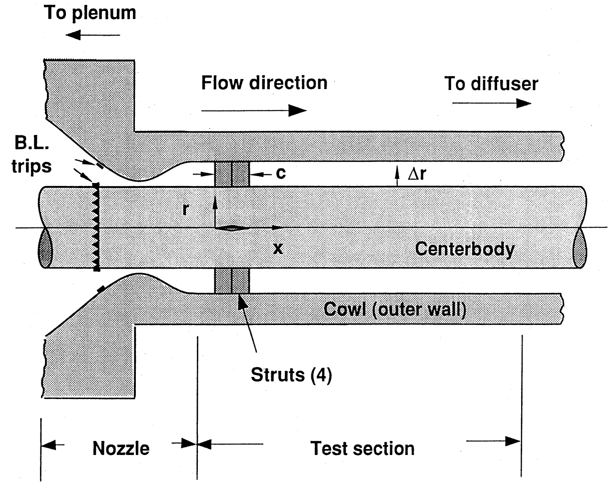

Fig. 2. Strut positions in annular duct.

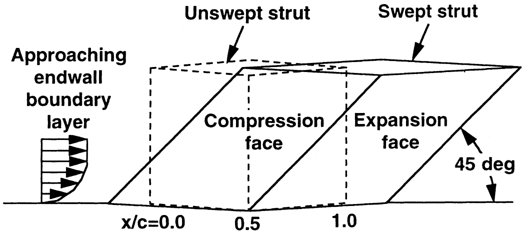

Fig. 3. Schematic of strut configurations.

Pitot pressure data were taken with two pitot tubes made from nested stainless steel tubing (0.30 mm tip diameter) designed to facilitate measurements near the cowl and centerbody. Wall static pressures were measured by means of wall taps having an orifice diameter of 0.34 mm. A cone-cylinder probe, 0.64 mm in diameter with a cone half-angle of 5°, was used for static pressure measurements in the flow. A family of two-tube Conrad probes was used to measure pitch and yaw angles in cross planes normal to the primary flow. Details of the probe configurations and data reduction procedures are given by Williams (1995). Experimental results in this paper are based on data taken at a location downstream of the strut trailing edge ($x/c = 4$, where x is measured from the strut leading edge as shown in Fig. 3). At this location pitot pressure and flow angle data were taken in radial increments of 0.5 mm over the annular gap width for a total of 35 measurements at each circumferential (θ) location. Static pressure data were also taken in radial increments of 0.5 mm, except near each endwall. Between the strut plane of symmetry ($\theta = 0°$) and the plane of symmetry between adjacent struts ($\theta = 45°$), pressure probe data were taken at 30 circumferential positions from 1° to 3° apart, depending on the amount of clustering needed to resolve the local shock structure. Data were also taken in 1° increments on either side of the wake centerline (at $\theta = 0°$) to check flow symmetry. Experimental data taken at $x/c = -0.5$ (0.5 chord lengths ahead of the strut leading edge) were used to initialize the computations. At this streamwise location the boundary layers on the cowl and centerbody surfaces were partially developed and fully turbulent, with a core flow Mach number of 2.9 and a Reynolds number based on chord width of 3×10^5. At this location the displacement and momentum thicknesses were nominally the same on each endwall ($\delta^* \approx 1.0$ mm, $\theta \approx 0.22$ mm).

3. Computational model

The equations of motion in strong conservation form were solved using NPARC (1994), which is an updated version of the PARC code (Cooper and Sirbaugh, 1989). Closure to this system of equations was effected by employing a combined version of the turbulence models proposed by Baldwin and Lomax (1978) and by Thomas (1979), as described in Appendix A, which is one of the options in NPARC. The grids for the calculations were created using GRIDGEN, as developed by Steinbrenner et al. (1990). Symmetry was invoked to limit the circumferential extent of the computational domain to a region between $\theta = 0°$ (strut plane of symmetry) and $\theta = 45°$ (plane of symmetry between adjacent struts). The grids for both the unswept and swept struts had $147 \times 75 \times 75$ nodes in the x, r, and θ directions, respectively, and were clustered near anticipated strut-induced shock locations. The grids extended to the strut, centerbody, and cowl surfaces, where no-slip, adiabatic wall conditions were specified. The first grid plane adjacent to each of these surfaces was located well within the viscous sublayer of the upstream boundary layer on each surface ($y^+ \leqslant 1$). Details of the computational procedure and the manner in which the composite turbulence model was implemented are given by Williams (1995). Further details also appear in the related paper by Williams and Gessner (1998).

4. Results and discussion

4.1. Shock structure

It is instructive to examine first the secondary shock structure induced at the strut/centerbody and strut/cowl intersections, inasmuch as compression and expansion waves generated at these locations impinge on the endwall boundary layers within which the leading and trailing edge horseshoe vortices are propagating. Fig. 4 shows computed shock and expansion wave behavior in the vicinity of the strut for both the unswept (Fig. 4(a)) and swept (Fig. 4(b)) strut configurations. As the leading edge shock wave generated by each strut configuration intersects the endwall boundary layers, expansion fans are formed which propagate radially away from the intersections. These expansion fans affect the flow by turning streamlines that have just crossed the leading edge shock wave away from the duct midheight toward the endwalls. Similarly, the expansion fan generated at the strut midchord interacts with the endwall boundary layers to generate shock waves that propagate away from the endwalls. These "intersection shocks" create a shock diamond pattern on the strut plane of symmetry behind the strut, as shown in the lower portion of Fig. 4. It will be shown shortly that when these weak shock waves interact with an endwall boundary layer downstream of the strut trailing edge, vorticity is reoriented and vortical flow patterns may develop in the interaction region.

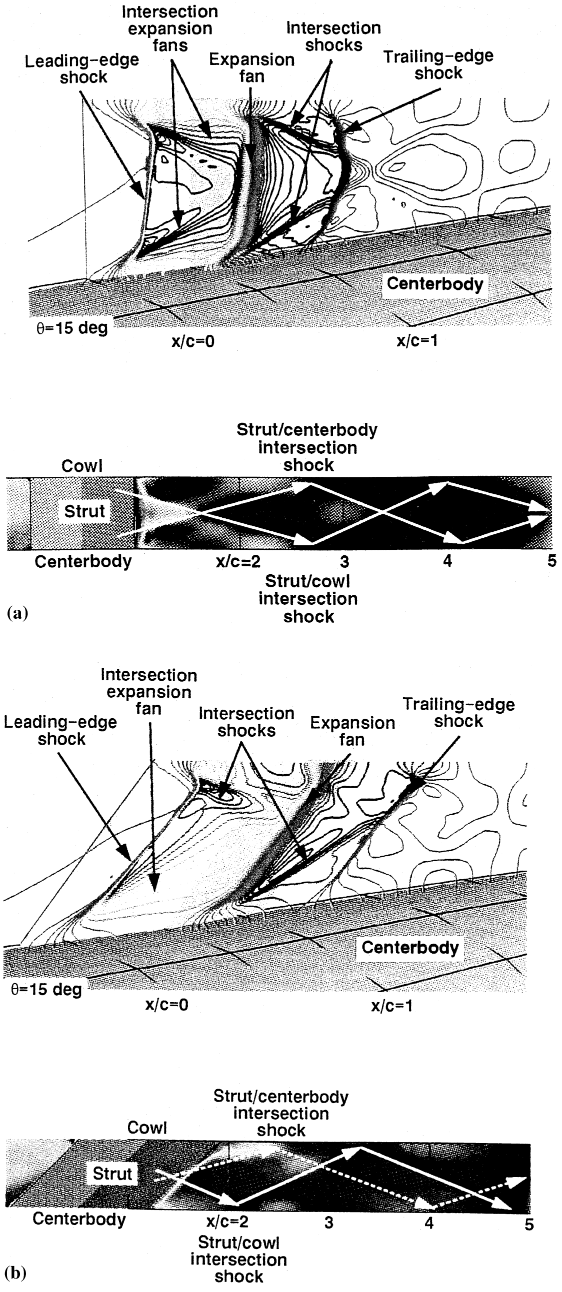

Fig. 4. Computed shock waves and expansion fans generated by strut/endwall intersections. (a) Unswept strut; (b) swept strut.

4.2. Limiting streamlines

Computed limiting streamlines on the cowl and centerbody surfaces are shown in Fig. 5 for both the unswept (Fig. 5(a)) and swept (Fig. 5(b)) strut configurations. The lines C1 and C2 are lines of coalescence (separation) which respectively bound the leading and trailing edge horseshoe vortices generated by the strut. The lines D1 and D2, where they appear, are lines of divergence (attachment) which also bound these vortices. The finite extent of the C and D lines in this figure should be interpreted only as a subjective measure of actual separation and attachment phenomena in the flow, inasmuch as these lines are

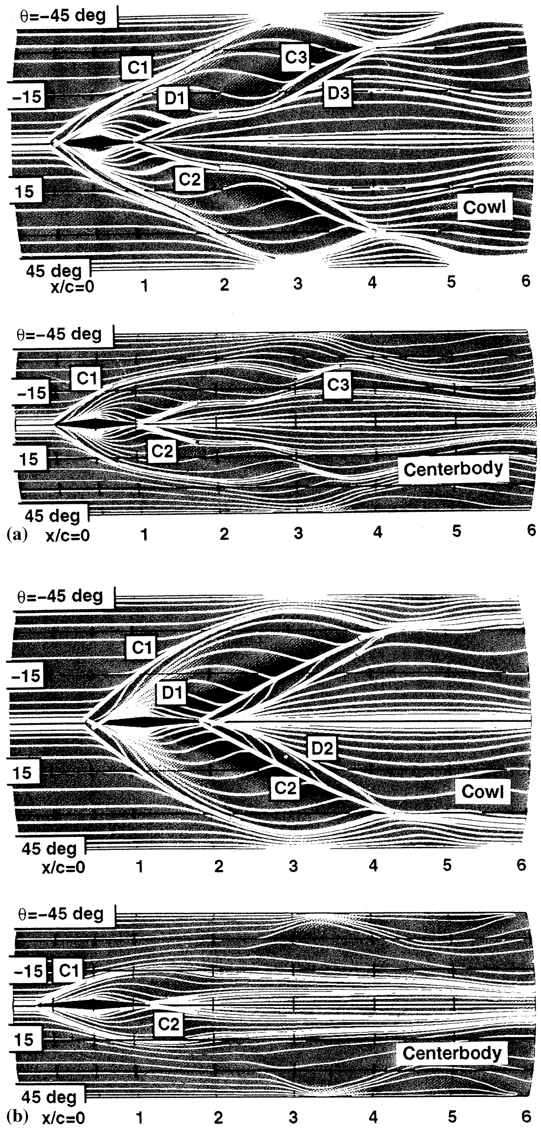

Fig. 5. Computed limiting streamlines on the cowl and centerbody surfaces. (a) Unswept strut; (b) swept strut.

not wholly representative of the actual flow because of inadequate grid resolution. For example, the computations show that the trailing edge horseshoe vortices on the cowl and centerbody surfaces maintain their integrity well downstream of the strut trailing edge (at least to $x/c = 5$), so that line C2 in Fig. 5(a) and (b) should extend over this distance for each strut configuration. Flow visualization results which depict this behavior are given by Williams (1995), but are not included in this paper, because black and white reproduction of the color photographs tends to obscure observed coalescence of the limiting streamlines.

One interesting feature of Fig. 5(a) is that lines C3 and D3 observed on the cowl for the unswept strut originate near $x/c = 3, \theta = \pm 15°$, which is at a position where the strut/centerbody intersection shock shown in Fig. 4(a) first impinges on the cowl. Fluorescent dye/oil flow visualization of limiting streamlines on the centerbody surface, in fact, shows that a crescent-shaped line of coalescence (C3) is formed downstream of each strut configuration that extends outward from the C2 line of coalescence which bounds the trailing edge horseshoe vortex (Williams, 1995). This behavior is not evident in computed limiting streamline behavior on the centerbody for the swept strut (Fig. 5(b)), again because of inadequate grid resolution. In contrast to this behavior, experimentally observed lines of coalescence which bound the compression corner face vortices that are propagating toward the center of the duct along the expansion face of each strut (refer to Fig. 1) are simulated well by the computations. More specifically, the computed lines of coalescence shown in Fig. 6 which bound these vortices (C4) are in good agreement with flow visualization results reported by Williams (1995).

4.3. Corner vortical flow structure

Cross flow vectors computed in the corner regions of the compression face/endwall intersections at 75% of the streamwise distance along the compression face of the strut are shown in Fig. 7. The vortex observed in each corner is bounded by lines of coalescence and divergence on the strut and endwall, as denoted by points C4 and D4, respectively, at this streamwise location. Inasmuch as the views in this figure are perspective views along computational grid lines which sweep downstream away from the strut, some of the bounding surfaces are canted as a result of three-dimensional effects. Although Fig. 7 shows that strut sweep has little effect on the size of the corner vortex bounded by the centerbody, the corner vortex bounded by the cowl for the swept strut is roughly twice as large as that for the unswept strut. This behavior is apparently the result of a relatively strong interaction induced by the intersection of the backward swept strut with the cowl (refer to Fig. 6(b)), which also induces a much stronger leading edge horseshoe vortex at the strut/cowl intersection compared to that observed for the unswept strut.

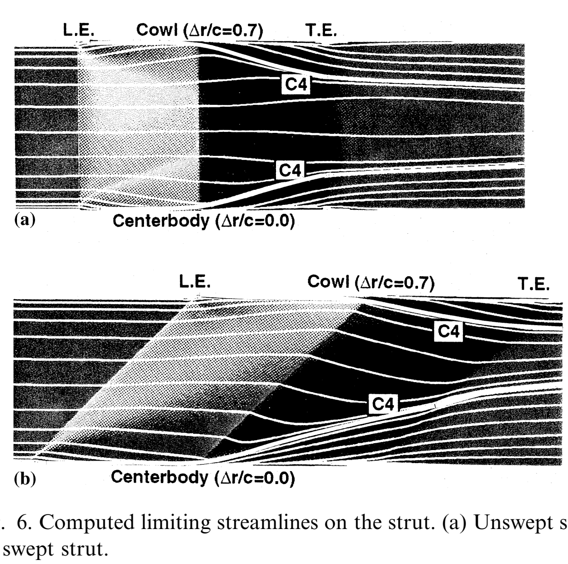

Fig. 6. Computed limiting streamlines on the strut. (a) Unswept strut; (b) swept strut.

Fig. 8 shows cross flow vectors and vortices computed in the corners of the expansion face/endwall intersections at 75% of the streamwise distance along the expansion face. The vortex in each corner is bounded by lines of coalescence and divergence, as denoted at this location by points C5 and D5, respectively. Note that the rotational sense of each expansion face corner vortex is opposite to that of its compression face counterpart (compare Figs. 7 and 8). For the unswept strut, a comparison of Figs. 7(a) and 8(a) shows that the magnitude of cross flow in the expansion face corner region is much larger than that observed in the compression face corner region at the same relative streamwise distance. For the swept strut, a comparison of Figs. 7(b) and 8(b) shows that the expansion face/cowl vortex is also much smaller than the compression face/cowl vortex. The expansion face corner vortices in Fig. 8 continue to migrate along the corners formed by the strut/endwall intersections until they eventually merge with horseshoe vortices generated at the strut trailing edge, as shown in

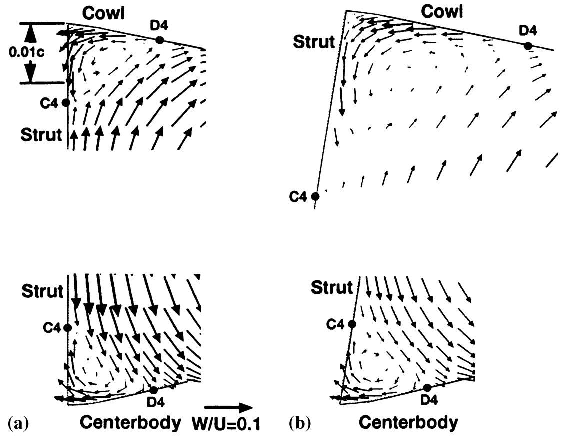

Fig. 7. Computed cross flow vectors near the compression face/endwall intersections. (a) Unswept strut; (b) swept strut.

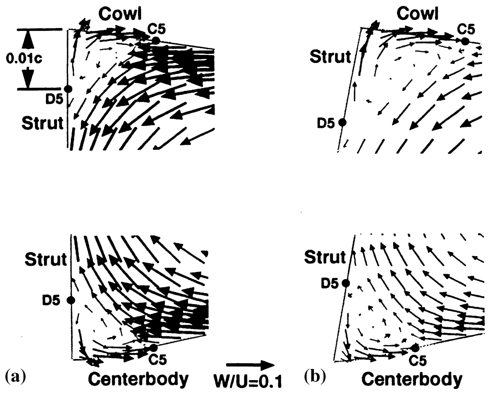

Fig. 8. Computed cross flow vectors near the expansion face/endwall intersections. (a) Unswept strut; (b) swept strut.

Fig. 1. In contrast, the compression face corner vortices shown in Fig. 7 migrate toward the duct midheight along the expansion faces of the strut, as shown schematically in Fig. 1, and as implied by the lines of convergence C4 shown in Fig. 6.

4.4. Cross-planar distributions

Pitot pressure contours and static pressure contours downstream of the swept strut trailing edge at $x/c = 4$ are shown in Figs. 9 and 10, respectively, where the static pressure (P) and pitot pressure (P_{t2}) contour levels have been normalized by the plenum pressure ($P_o = 1030$ Torr). The measured results within the circumferential interval $-6° \leqslant \theta \leqslant 6°$ are indicative of the level of symmetry observed about $\theta = 0°$ in the experimental flow. In general, Figs. 9 and 10 show that there is close correspondence between measured and computed distributions for each variable, except in the wake region centered about $\theta = 0°$. The concentration of steep gradients in the central region of the flow near $\theta = 22°$ and 36° correspond, respectively, to the circumferential positions of the trailing edge shock and of the crossing leading edge shock from the neighboring strut at $\theta = 90°$.

Computed and measured cross flow vectors at $x/c = 4$ are shown in Fig. 11. Again, computed and measured distributions outside the wake region agree very well. The relatively strong, inwardly directed cross flow at $\theta = 30°$ near each endwall is due primarily to the crossing shock from the neighboring strut which has entered the flow domain and has a relatively strong influence on the endwall boundary layers at this location. The inwardly directed vectors near the cowl and centerbody are compatible with the limiting streamlines for the swept strut shown in Fig. 5(b), which are canted on each surface toward the strut plane of symmetry at, and near, $x/c = 4, \theta = 30°$. Examination of Fig. 9 shows that discrepancies between computed and measured pitot pressures exist in the wake region behind the strut. This can be seen more clearly in Fig. 12, which is a circumferentially expanded view at the results in Fig. 9 centered about $\theta = 0°$. Fig. 12 shows that both the width of the wake and the level of distortion in the wake are underestimated by the computations. The measured contour variations between $\Delta r/c = 0.2$ and 0.3 near $\theta = 0°$ are the direct result of a vortex pair corresponding to two, contra-rotating vortices generated at the compression face/centerbody intersection that are propagating in the wake region. Analysis of cross flow data taken in this region has shown that these vortices are roughly centered at $\Delta r/c = 0.27, \theta = \pm 2°$ (Williams, 1995). The measurements did not reveal, however, whether vortices generated at the compression face/cowl intersection actually exist in the flow at $x/c = 4$, although their presence at this location was confirmed experimentally for the unswept strut. The point to note here is that the computed pitot pressure contours in Fig. 12(b) are relatively undistorted in the same region where vortex-induced distortion is observed experimentally, because the prescribed isotropic eddy viscosity turbulence model does not predict the presence of corner induced vortices in the wake region behind a strut. This shortcoming should be addressed in future work by developing a more representative turbulence model for the wake region.

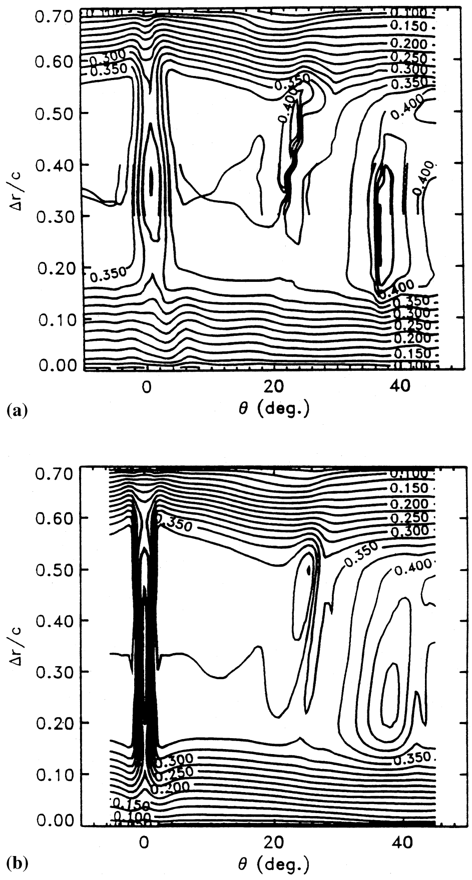

Fig. 9. Pitot pressure (P_{t2}/P_o) contours at $x/c = 4$. (a) Measured; (b) computed.

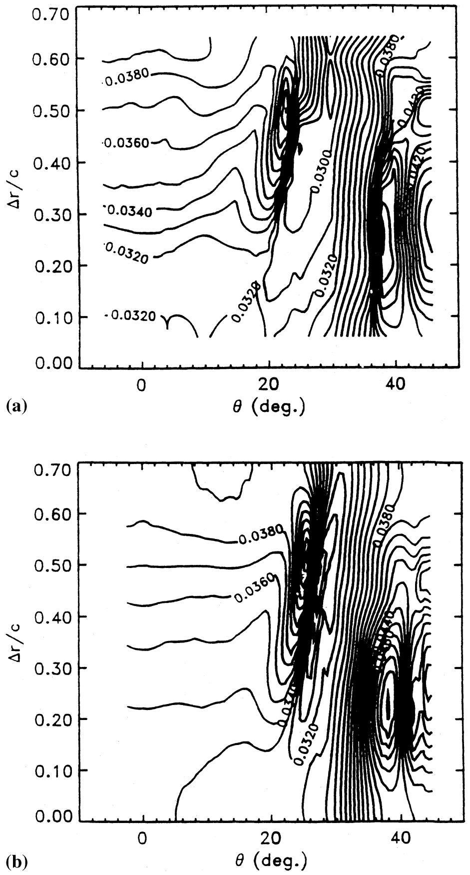

Fig. 10. Static pressure (P/P_o) contours at $x/c = 4$. (a) Measured; (b) computed.

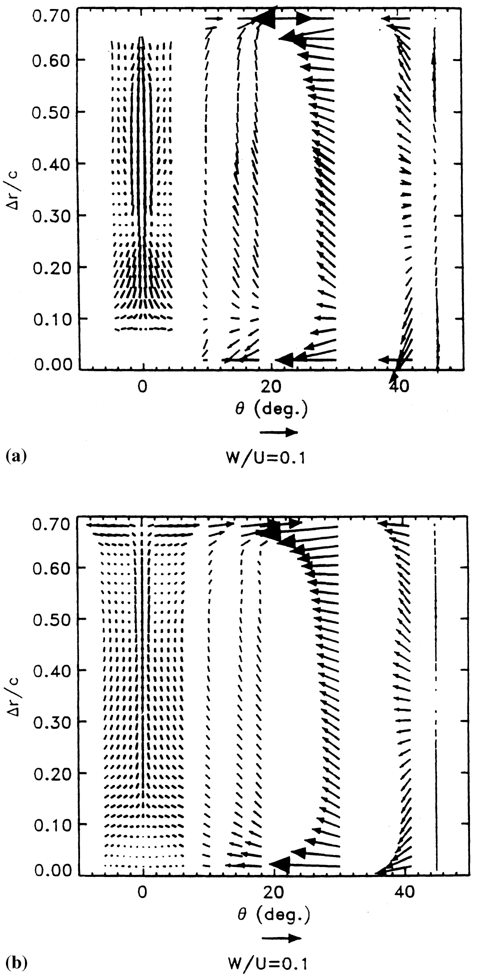

Fig. 11. Cross flow vectors at $x/c = 4$. (a) Measured; (b) computed.

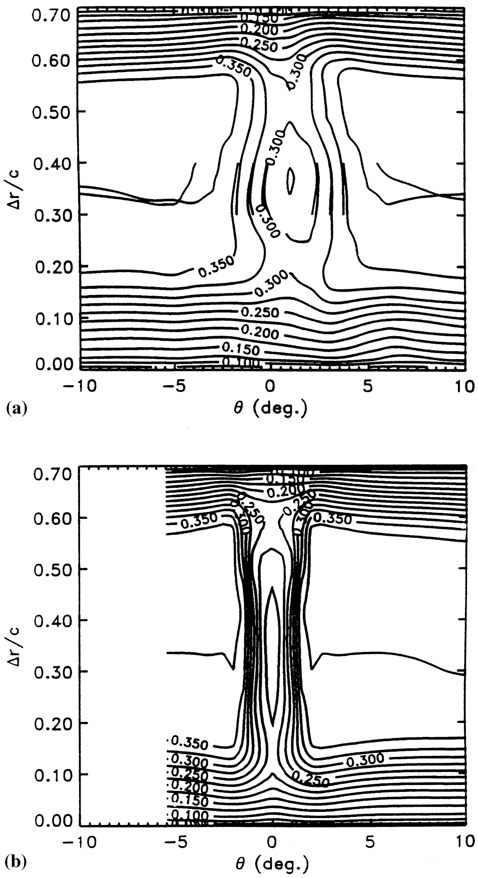

Fig. 12. Pitot pressure (P_{t2}/P_o) contours in the wake region at $x/c = 4$. (a) Measured; (b) computed.

5. Concluding remarks

This paper has presented the results of a study related to the effect of strut sweep on the nature of supersonic flow past diamond-shaped struts mounted on a circular centerbody positioned concentrically within a circular cowl. Computed results which compare shock structure, limiting streamline patterns, and cross flow vector behavior for both unswept and swept struts show that the local flow structure near, and downstream of, each strut/endwall intersection is basically similar, with some observed differences between the size and strength of corner-induced vortices along the intersection. Comparisons between measured and computed distributions downstream of the swept strut-trailing edge show that the prescribed turbulence model is performing properly, except in the wake region behind the strut. Further work on model development is needed in order to improve predictive capabilities in this region.

Acknowledgements

This study was supported by a grant from the NASA-Lewis Research Center (NAG3-376). Dr. David O. Davis was the project monitor. The computations were performed on the NAS Cray Y-MP computer at NASA Ames and the Cray Y-M computer at NASA-Lewis. The authors would like to express their appreciation to NASA for its support of their research.

Appendix A

Closure to the conservation equations was obtained by employing an algebraic turbulence model based on the Baldwin–Lomax (B–L) model (1978) in combination with the P.D. Thomas (PDT) model (1979). The effect of turbulence is introduced into the equations through the variables μ_{total} and k_{total}, which are defined as

$$\mu_{\text{total}} = \mu + \mu_\tau \tag{A.1}$$

and

$$\frac{k_{\text{total}}}{Pr} = \frac{k}{Pr} + \frac{\mu_\tau}{Pr_\tau}, \tag{A.2}$$

where k is the thermal conductivity normalized by a reference value, Pr is the Prandtl number, and μ_τ and Pr_τ are the "turbulent" viscosity and Prandtl numbers, respectively. The turbulent Prandtl number was assumed to be uniform and equal to 0.9 throughout the flowfield. Turbulent viscosities were determined for two regions: an inner (wall-bounded) region and an outer (unbounded) region. The turbulent viscosity for the inner region was calculated from the B–L inner region model:

$$\mu_\tau = \rho \ell^2 \left| \vec{\omega} \right|, \tag{A.3}$$

where

$$\vec{\omega} = \nabla \vec{u}, \tag{A.4}$$

and where

$$\ell = \kappa y[1 - \exp(-y^+/A^+)] \tag{A.5}$$

with y defined as the local wall coordinate. The van Driest constant, A^+, and von Karman constant, κ, were set to equal 26 and 0.4, respectively. In corner regions, the turbulent viscosity was calculated as an average of the two viscosities determined relative to each wall, namely

$$\mu_\tau = \frac{(\mu_{\tau,j}/y_j) + (\mu_{\tau,k}/y_k)}{\left((1/y_j^2) + (1/y_k^2)\right)^{1/2}}. \tag{A.6}$$

The turbulent viscosity in the outer region was taken to be the maximum value calculated from the B–L and PDT outer region models, namely

$$\mu_\tau = \max\left\{ \begin{matrix} \mu_{\tau\text{B–L}} \\ \mu_{\tau\text{PDT}} \end{matrix} \right\}. \tag{A.7}$$

The turbulent viscosity calculated by the B–L outer region model, $\mu_{\tau\text{B-L}}$, is defined as

$$\mu_{\tau\text{B-L}} = K C_{\text{cp}} \rho F_{\text{wake}} F_{\text{Kleb}}(y), \tag{A.8}$$

where

$$F_{\text{wake}} = \min\left\{ \begin{matrix} y_{\max} F_{\max} \\ C_{wk} y_{\max} (u^2 + v^2 + w^2)_{\max} / F_{\max} \end{matrix} \right\}. \tag{A.9}$$

The subscript max represents the location of the maximum value of F, which is defined as

$$F = y|\omega'|[1 - \exp(-y^+/A^+)]. \tag{A.10}$$

The Klebanoff intermittency factor, F_{Kleb}, is defined by

$$F_{\text{Kleb}} = \left[1 + 5.5(y C_{\text{Kleb}}/y_{\max})^6\right]^{-1}, \tag{A.11}$$

where, in reference to Eqs. (A.8)–(A.11), $K = 0.0168$, $C_{\text{cp}} = 1.6, C_{\text{wk}} = 0.25$, and $C_{\text{Kleb}} = 0.3$. The vorticity variable, ω', used to calculate the F function from Eq. (A.10), is the component of the vorticity vector parallel to the wall and normal to the velocity vector. The turbulent viscosity calculated by the PDT outer region model, $\mu_{\tau\text{PDT}}$, is defined as

$$\mu_{\tau\text{PDT}} = \rho \ell^2 \left|\vec{\omega}\right|, \tag{A.12}$$

where the mixing length ℓ is calculated from

$$\ell = \frac{\ell_o[\max(\left|\vec{u}\right|) - \min(\left|\vec{u}\right|)]}{\left|\vec{\omega}_c\right|} \tag{A.13}$$

$|\vec{\omega}_c|$ is the value of the maximum magnitude of the vorticity, and ℓ_o is a coefficient prescribed as

$$\ell_o = \min\left\{ \begin{matrix} \ell_c \\ 0.09 \end{matrix} \right\}, \tag{A.14}$$

where ℓ_c is an adjusted coefficient which models compressibility effects and is defined in terms of the local Mach number M as

$$\ell_c = \max\left\{ \begin{matrix} \left(\frac{0.12}{1+0.3M^2}\right) \\ 0.0564 \end{matrix} \right\}. \tag{A.15}$$

The composite B–L and PDT turbulence model prescribed in this study has been shown to predict flowfields with combined wall-bounded and free shear regions more accurately than either model independently (NPARC, 1994).

References

Baldwin, B.S., Lomax, H., 1978. Thin layer approximation and algebraic model for separated turbulent flows. AIAA Paper 78–257.

Barnhart, P.J., 1988. A preliminary design study of supersonic through-flow fan inlets. AIAA Paper 88–3075.

Cooper, G.K., Sirbaugh, J.R., 1989. PARC code: theory and usage, AEDC-TR-89-15. Arnold Engineering Development Center.

Franciscus, L.C., 1987. The supersonic through-flow turbofan for high mach propulsion. AIAA Paper 87–2050.

Heiser, W.H., Pratt, D.T., 1993. Hypersonic Airbreathing Propulsion. AIAA Publications, New York.

NPARC 1.2a User Notes, 1994. Arnold Engineering Development Center.

Rizzetta, D.P., 1995. Numerical simulation of oblique shock-wave/vortex interaction. AIAA J 33 (8), 1441–1446.

Smart, M.K., Kalkhoran, I.M., 1995. Effect of shock strength on oblique shock wave/vortex interaction. AIAA J 33 (11), 2137–2143.

Steinbrenner, J.P., Chawner, J.R., Fouts, C.L., 1990. The Gridgen 3D multiple block grid generation system, WRDC-TR-90-3022, vols. 1&2. Wright-Patterson Development Center.

Thomas, P.D., 1979. Numerical method for predicting flow characteristics and performance of nonaxisymmetirc nozzles-theory. NASA CR 3147.

Williams, K.E., 1995. Investigation of supersonic flow about strut/endwall intersections in an annular duct. Ph.D. Thesis, Department of Mechanical Engineering, University of Washington, Seattle, WA.

Williams, K.E., Gessner, F.B., 1996. On the evolution of strut-induced vortices in supersonic annular flow. AIAA Paper 96–0324.

Williams, K.E., Gessner, F.B., 1998. Flowfield characteristics of struts in supersonic annular flow. Exp. Therm. Fluid Sci. 17 (1 & 2), 156–164.

Williams, K.E., Gessner, F.B., Harloff, G.J., 1994. Design and operation of a supersonic annular flow facility. AIAA J 32 (7), 1528–1531.

Williams, K.E., Harloff, G.J., Gessner, F.B., 1995. Investigation of supersonic flow about strut/endwall intersections. AIAA J 33 (4), 586–594.